Research Article

Construction of Te-ZnO@S-g-C$_3$N$_4$ Heterojunction Nanocomposites for the Efficient Removal of Methylene Blue, Antifungal Activity, and Adsorption of Cr(VI) Ion

Komal Aroosh,[1] Mohsin Javed,[1] Nadia Hussain,[2,3] Ahmad Alhujaily,[4] Shahid Iqbal [ORCID],[5] Mohammed T. Alotaibi,[6] Muhammad Faizan,[1] Muhammad Shuaib Khan,[7] Ali Bahadur [ORCID],[8] Muhammad Abdul Qayyum,[9] Nasser S. Awwad,[10] Yosef Jazaa,[11] Foziah F. Al-Fawzan [ORCID],[12] and Eslam B. Elkaeed [ORCID][13]

[1]Department of Chemistry, School of Science, University of Management and Technology, Lahore 54770, Pakistan
[2]Department of Pharmaceutical Sciences, College of Pharmacy, Al Ain University, Al Ain, UAE
[3]AAU Health and Biomedical Research Center, Al Ain University, Abu Dhabi, UAE
[4]Biology Department, College of Science, Taibah University, Al Madinah Al Munawwarah 41477, Saudi Arabia
[5]Department of Chemistry, School of Natural Sciences (SNS), National University of Science and Technology (NUST), H-12, Islamabad 46000, Pakistan
[6]Department of Chemistry, Turabah University College, Taif University, P.O. Box 11099, Taif 21944, Saudi Arabia
[7]State Key Laboratory of Catalysis, iChEM, Dalian Institute of Chemical Physics, Chinese Academy of Sciences, Dalian National Laboratory for Clean Energy, Dalian, 116023 Liaoning, China
[8]Department of Chemistry, College of Science and Technology, Wenzhou-Kean University, Wenzhou 325060, China
[9]Department of Chemistry, Division of Science & Technology, University of Education, Lahore, Pakistan
[10]Chemistry Department, Faculty of Science, King Khalid University, P.O. Box 9004, Abha 61413, Saudi Arabia
[11]Faculty of Engineering, King Khalid University, P.O. Box 9004, Abha 61413, Saudi Arabia
[12]Department of Chemistry, College of Science, Princess Nourah bint Abdulrahman University, P.O. Box 84428, Riyadh 11671, Saudi Arabia
[13]Department of Pharmaceutical Sciences, College of Pharmacy, AlMaarefa University, Riyadh 13713, Saudi Arabia

Correspondence should be addressed to Foziah F. Al-Fawzan; ffalfozan@pnu.edu.sa

Heterojunctions have proven to be effective catalysts for removing organic pollutants and heavy metals from wastewater. The following study is also about the formation of 2D heterojunction tellurium-doped zinc oxide composite with sulfur-doped graphitic carbon nitride (Te-ZnO@S-g-C$_3$N$_4$) by adopting a low-cost, simple, and ecofriendly coprecipitation technique. Thiourea was calcined to prepare S-g-C$_3$N$_4$ using the thermal degradation method. The characterization of synthesized photocatalysts was carried out by using SEM-EDX, FTIR, and XRD. The results obtained showed that the incorporation of tellurium caused an alteration in the wurtzite structure of ZnO. SEM-EDX analysis validated the purity of the synthesized samples due to the absence of any additional peaks. The decrease in the bandgap was also noted by the formation of composites. Using methylene blue as a reference dye, the UV-vis spectrophotometer was utilized to calculate the absorbance for photocatalytic degradation behavior. As a result of tellurium doping into the ZnO lattice, photocatalytic oxidation/reduction was improved, according to the results. 3Te-ZnO NPs showed the best degradation rate among dopant series, while an excellent overall degradation rate was noted by fabricated composite 3Te-ZnO@40S-g-C$_3$N$_4$. The best doped ZnO and

composites were also used as sorbents for the abstraction of heavy metal (Cr(VI)) from water via adsorption. A definite rise in the removal efficiency percentage of chromium ions was observed by using these sorbents. The overall photo degradation rate and adsorption behavior noted were in ZnO<Te-ZnO<Te-ZnO@S-g-C_3N_4 order. When compared to ZnO, Te-ZnO, SCN, and Te-ZnO@40SCN, the 3Te-ZnO@40SCN NCs have outstanding antifungal potential. The improved dispersibility and interaction of 3Te-ZnO@40SCN with membrane and intracellular proteins of fungi may be the cause of the greater effect of Te-ZnO@40SCN.

1. Introduction

Unpredictable climate change and an increase in human population have recently resulted in the crisis of clean water supply for both people and wildlife [1, 2]. Moreover, dye emission from various sectors is another issue that contaminates water and has drawn a lot of attention [3]. The effluents obtained from the printing industry and textile dyeing are complex and contain dissolved and suspended solids, organic compounds, and heavy metals [4]. Since azo dyes do not stick to the cloth during the dyeing process, 15 to 50 percent of them are washed away with the wastewater. This wastewater is employed in irrigation procedures even though it is not beneficial for crop germination or growth [5–7]. Textile dyes also cause mutations and generate cancer-causing agents [8]. A kind of basic cationic dye that is widely used by many industries is methylene blue (MB). Shock, tissue necrosis, cyanosis, vomiting, and jaundice become more common in affected individuals [8]. Dyes decrease the light penetration in water, thus affecting the photosynthesis process [9]. Therefore, it surely needs to remove these dyes from the wastewater. To treat contaminated effluents, several physical, chemical, and biological techniques have been employed. The photocatalytic degradation of organic pollutants utilizing nanoparticles as the photocatalyst is one of the environmentally friendly methods for treating industrial effluent.

The photocatalysis mechanism involves the conversion of toxic pollutants into nontoxic ones through light irradiation [10]. A wide range of semiconductor photocatalysts (e.g., TiO_2 [11–15], ZnO [1], CuO [16], NiS [17], SnO_2 [18], ZrO_2 [19], and WO_3 [20]) with various nanostructures have been studied. At ambient temperature, ZnO has a relatively wide bandgap of about 3.37 eV, an excitation energy of about 15 meV, and a significantly high excitation binding energy of around 60 meV. It is a transparent, dielectric, and piezoelectric semiconducting oxide [21]. It is observed from previous studies that the photoactivity of bare ZnO is limited due to the instant recombination of photogenerated e^--h^+ pairs, photocorrosion, and visible light inactiveness [22]. Metal doping enhances the photocatalytic efficiency of ZnO. By introducing impurities between energy levels in the form of a midgap state, doping aids in the reduction of the bandgap. Dopants can alter the size of the grain and its corresponding surface area, as well as cause structural and microstructural flaws [23–25]. The doping of tellurium (Te) in zinc oxide (ZnO) can tailor its (ZnO) luminescence properties through the passivation of oxygen defects [26–28]. It has been reported that on doping of ZnO, the bond length between Zn and O will change due to stretching vibrations and shifting to lower and higher energy regions. The bond length value between Zn and O will also decrease at high levels of Te doping and increase at low doping concentrations [29]. Te-ZnO photocatalytic efficiency still falls short of expectations. To increase its catalytic efficiency, it can be coupled with a suitable polymeric molecule. g-C_3N_4 may be a helpful semiconductor for integrating with other semiconductors, notably ZnO, because of its suitable bandgap (2.7 eV) and absorption in the visible spectrum of light [30–33]. The nitrogen incorporated in carbon nitride helps to capture more visible light because of its lower electronegativity and higher potential energy compared to oxygen [1]. It has been thoroughly investigated as a practical, stable, affordable, and safe photocatalyst to address the pollution concerns.

Up to now, several reports on the metal doping in ZnO have been demonstrated, which showed an increase in the photocatalytic degradation rate as compared to ZnO [34]. Jamali-Sheini et al. revealed morphological and structural changes due to the Te doping into ZnO. Shanmugam et al. reported the improved photodegradation efficiency of brilliant green (BG) by employing Te-doped ZnO nanosheets. Sher et al. loaded Mo-ZnO on g-C_3N_4 nanosheets in order to obtain superior photocatalytic efficiency against MB [35]. Ahmad et al. reported that Ag-doped ZnO nanoparticles are efficient photocatalysts to photodegrade methyl orange, rhodamine B, and safranine O in a short time [36]. Equally, the doped metal oxide coupling on g-C_3N_4 sheets has been stated to demonstrate the improved photocatalytic behavior. Sher et al. and Kuang et al. designed a highly effective g-C_3N_4/Sn ZnO photocatalyst that showed an improvement in the photocatalytic effectiveness of MB from 35 to 88% [37, 38]. Qamar et al. reported 100% degradation of MB by using g-C_3N_4/Co@ZnO under sunlight [39]. Zhang et al. reported 98.97% of MB degradation by using a novel ternary nanocomposite (Ag/g-C_3N_4/$LaFeO_3$). In order to degrade Rh-B under the influence of visible light, Zhang et al. synthesized g-C_3N_4/MoS_2/grapheme nanocomposite that shows a photodegradation rate nearly 4.8 times superior to that of pristine g-C_3N_4 [40].

Inspired by the improved photocatalytic performance of metal-doped ZnO and ZnO/S-g-C_3N_4, we fabricated Te-ZnO and Te-ZnO/S-g-C_3N_4 via the ecofriendly coprecipitation technique. Thiourea was polycondensed to produce S-g-C_3N_4. Using a model dye, the photocatalytic characteristics of manufactured catalysts were investigated (MB). The subsequent investigation was divided into two parts. Phase 1 of the investigation looked at the photocatalytic capability of Te-doped zinc oxide NPs (1, 3, 6, 9, 12, and 15 wt%). The greatest dye degradation rate/efficiency was achieved by the 3 percent Te-ZnO NPs (3 Te-ZnO). The 3 percent Te-ZnO NPs were combined with S-g-C_3N_4 (SCN) concentrations of 20, 40, 60, and 80 weight percent in the second phase to create Te-ZnO/S-g-C_3N_4 NCs, which further increased the photocatalytic activity. In comparison to other samples, the 3Te-ZnO@40SCN

nanocomposite (3Te-ZnO@40SCN) had the best photocatalytic activity. The synthetic materials might find use in the wastewater treatment industry. Furthermore, nanocomposite uses are not restricted to the purification of wastewater/dye water. They can also be used to fabricate energy storage and conversion devices due to their environmentally pleasant nature [41, 42].

2. Materials and Methods

2.1. Reagents. The zinc chloride ($ZnCl_2$), tellurium (Te), methylene blue, ammonia (NH_3), potassium dichromate, polyethylene glycol, and thiourea (CH_4N_2S) were bought from Merck and employed as such.

2.2. Synthesis of Undoped ZnO and Te-Doped ZnO NPs. In a typical ZnO synthesis experiment, 200 ml of distilled water was used to dissolve 3.38 g of ZnCl2 and 4 ml of polyethylene glycol. NH_3 (4 ml) was added dropwise and stirred continuously for two hours, causing white precipitates to develop (a milky solution). The precipitates were collected, repeatedly rinsed in a water/ethanol solution, and then dehydrated in an oven for two hours at roughly 80°C. Then, calcination of the precipitates was carried out at 400°C in a muffle furnace for 3 hours. Finally, precipitates were ground and stored. A series of Te-doped ZnO nanoparticles (1, 3, 6, 9, 12, and 15 wt%) were synthesized by the same process except with the addition of various concentrations of tellurium.

2.3. Fabrication of SCN. For the synthesis of S-g-C_3N_4 nanosheets, 10 g of the thiourea was taken in a covered crucible and placed in a muffle heating system to carry out the calcination. The temperature was gradually increased at a rate of 5°C per minute until it reached 550°C and kept there for about 4 hours [43]. The obtained yellowish product was permitted to cool at room temperature, ground into a fine powder, and then stored safely.

2.4. Synthesis of Nanocomposites (Te-ZnO@SCN). For the preparation of 20, 40, 60, and 80% nanocomposite series, 3% Te-doped ZnO nanoparticles were hybridized with 0.005, 0.13, 0.26, and 0.39 g of S-g-C_3N_4, respectively. In a typical synthesis of 20% nanocomposites, 0.13 g of Te powder was added into a 0.1 M solution of $ZnCl_2$ under magnetic stirring. To induce precipitation, 4 mL NH_3 was added dropwise to the solution, whereas 4 mL polyethylene glycol was added to avoid agglomeration. This solution is marked as solution A. Subsequently, the required S-g-C_3N_4 was ultrasonically dispersed into 50 ml water to prepare solution B. After that, the two solutions were combined into a single beaker and swirled for around two hours at room temperature. The precipitates were dehydrated in an oven at 80°C for two hours after filtering and washing with water/ethanol. In a muffle furnace, the precipitates were calcined for roughly three hours at 400°C. The finished product was powdered down to a fine consistency.

3. Results and Discussion

3.1. Bandgap Determination: Optical Property. The UV-visible spectroscopy was used to measure the absorbance of the fabricated samples that were further used to draw the "Tauc plot." The calculated bandgaps for ZnO NPs and g-C_3N_4 NSs were 3.13 and 2.32 eV, respectively, as shown in Figures 1(a) and 1(b). These bandgaps obtained were similar to the previously reported work [44–46]. These bandgap values indirectly confirmed the successful synthesis of the desired ZnO and SCN. The bandgap of 3Te-ZnO NPs was calculated to be 2.59 eV (Figure 1(c)), indicating that doping reduced the bandgap of ZnO. Tellurium (Te) doping on ZnO can tailor its luminous properties by passivation oxygen defects [27–29, 47]. The bandgap of Te-ZnO@40SCN was calculated as 2.10 eV (Figure 1(d)), indicating that hybridization with SCN further lowered the bandgap of ZnO. In order to make ZnO a more efficient photocatalyst in visible light, the bandgap narrowing showed that ZnO hybridization reduced the bandgap and shifted its light-absorbing ability toward the visible portion of the light spectrum (red shift) [48].

3.2. Validation of Functional Group by FTIR Spectrum. To confirm the functional groups of the manufactured samples, FTIR spectroscopy was performed to characterize them (Figure 2). The FTIR spectra of ZnO showed the fundamental mode of vibration at around 3492 cm^{-1} due to O-H stretching [49]. For 3% tellurium-doped ZnO, a peak around 3503 cm^{-1} was observed that indicated stretching vibrations of the -OH group due to the presence of moisture/water. Weak bands for Te-ZnO NDP in the 611-1518 cm^{-1} range are a sign that Te^{4+} ions were successfully incorporated into the ZnO NPs. These peaks obtained are almost similar to the absorption band observed for ZnO NPs, with a slightly higher wavenumber cm^{-1}. SCN's FTIR spectra showed a distinct absorption band at 808 cm^{-1}, which is connected to the triazine group's stretching vibration. The existence of C-N heterocycles that have undergone vibrational stretching is indicated by the absorption bands that were detected in the 1228-1616 cm^{-1} range. The water molecule adsorbed and N-H vibration probability associated with uncondensed amine groups are represented by the characteristic band at 3111 cm^{-1} [43].

These spectra's peaks coincide with previously published research. The precise absorption bands at 3476, 2986, 1381, 1036, 885, and 718 cm^{-1} were seen in the composite spectra like the peaks in 3Te-ZnO, while the peaks at 808, 1336, and 1544 cm^{-1} resemble the absorption bands found in SCN spectra. It confirms the successful synthesis of 3Te-ZnO@SCN nanocomposite. An increase in the transmittance percentage was observed by the incorporation of Te-doped NPs into SCN.

3.3. Structural Confirmation by X-Ray Diffractograms. The phase, purity, and lattice characteristics of the produced nanocatalysts (ZnO, SCN, and Te-ZnO@40SCN) were characterized by XRD. The XRD pattern of zinc oxide showed peaks at $2\theta° = 32.29°$, 34.94°, 36.77°, 48.04°, 57.08°, 63.33°, 66.89°, 68.41°, 69.52°, 77.03°, and 77.45° which
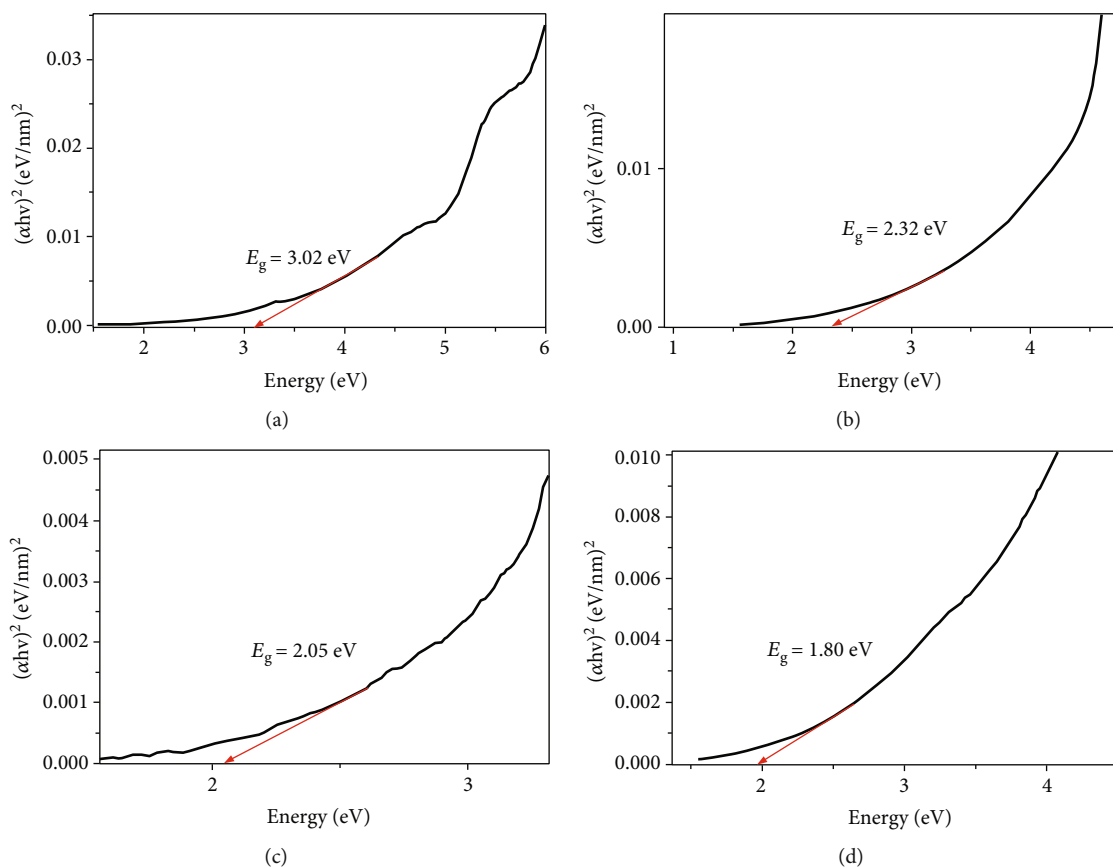
FIGURE 1: Bandgap estimation of (a) ZnO, (b) Te-ZnO, (c) SCN, and (d) Te-ZnO@SCN by employing the Tauc plot.

correspond to (100), (002), (101), (102), (110), (103), (200), (112), (201), (004), and (202) crystalline planes of ZnO (Figure 3(a)). All these peaks or characteristics of the Miller indices validate the wurtzite structure of ZnO. The result obtained was the same as the previously reported work [29, 36, 50, 51]. Indicating the successful doping of Te into ZnO and the coupling of SCN with Te-ZnO photocatalysts, the X-ray diffraction patterns of 3Te-ZnO and Te-ZnO/ 40%SCN exhibit a little shift toward the lower angle (Figure 3(b)). This discovery shows that Te^{4+} has successfully replaced Zn2+ in the ZnO lattice [29, 52].

Figure 3(c) displays the XRD form for S-g-C_3N_4 containing the two distinct peaks at 13.02° and 27.3° which correspond to the (100) and (002) facets of the crystals. These two peaks are probably due to the interplanar tri-s-triazine unit and the coupled aromatic arrangement, respectively. In the XRD findings of Te-ZnO/40%SCN, the crystal planes (100) and (002) are due to the peaks at 11.67° and 27.97° confirming the presence of S-g-C_3N_4 while the peaks appearing (32.25°, 34.8°, 36.7°, 48.0°, 57.0°, 63.3°, 66.8°, 68.4°, 69.4°, 72.9°, and 77.3°) correspond to the crystalline planes of tellurium-doped ZnO. The intensity of all these peaks is slightly lower as compared to peaks present in ZnO and tellurium-doped zinc oxide diffractograms, which indicate successful synthesis of Te-doped zinc oxide composite with SCN (Figure 3(d)).

3.4. SEM-EDX Analysis. The morphological structure and corresponding elemental makeup of ZnO, Te-ZnO NPs, and Te-ZnO@SCN NCs are described using SEM-EDX images in Figures 4(a)–4(f). ZnO NPs exhibited porous morphology with particle widths in the range of 100–600 nm, but these NPs had an average particle size of ~291 nm (Figure 4(a)). Zn and O peaks are present in the ZnO EDX spectrum, indicating that the NPs are pure (Figure 4(b)). The particles have a rod-like shape with a preferential horizontal orientation. The Te-ZnO NPs are showing a disordered rod-like structure (Figure 4(c)). In EDX spectrum of Te-ZnO, peaks for the Te, Zn, and O elements are seen (Figure 4(d)). The rod structures of these NPs are more stacked together than ZnO NPs forming the agglomeration. This agglomeration is due to the reduction of the combined total surface energy of all the particles. The average width recorded for these nanorods is 300 nm. The Te-ZnO@SCN NCs' morphology is seen in Figure 4(e). The elemental peaks for sulfur, carbon, nitrogen, zinc, oxygen, and Te can be seen in the EDX spectrum of Te-ZnO@SCN NCs, which is oriented haphazardly on the surface of the SCN sheets in NCs (Figure 4(f)). No additional peak was present, confirming the purity of the synthesized samples.

3.5. XPS Analysis. XPS measurements were used to look into the constituent elements' chemical states and composition in
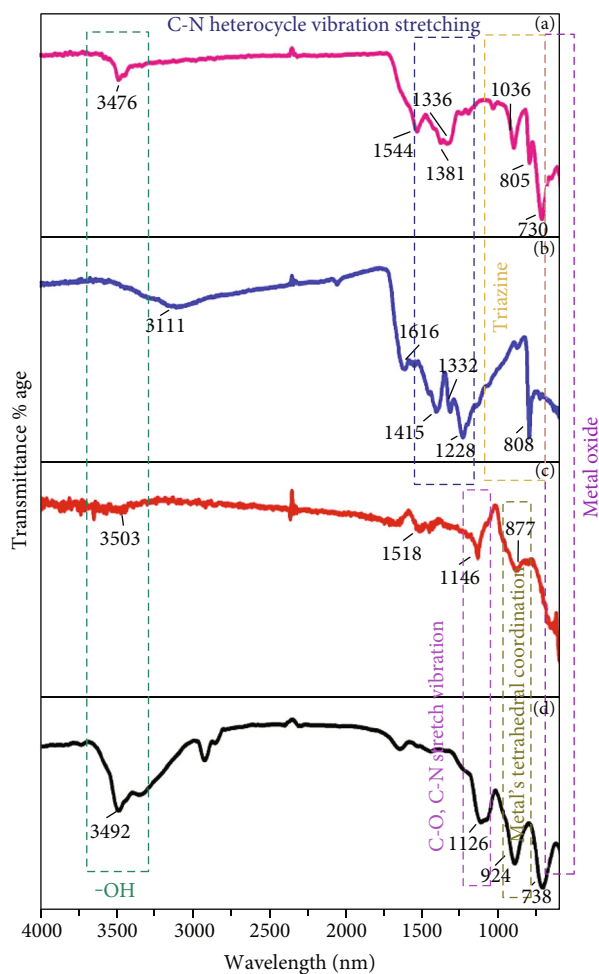
FIGURE 2: FTIR spectrum of (a) ZnO, (b) Te-ZnO, (c) SCN, and (d) Te-ZnO@SCN.

FIGURE 3: XRD pattern of (a) ZnO, (b) Te-ZnO, (c) SCN, (d) Te-ZnO@SCN, and (e) shifting of angles.

the 3Te-ZnO@40SCN NCs. The deconvolution Zn 2p spectrum in Figure 5(a) exhibits two distinct Zn^{2+} peaks at 1021.82 and 1044.76 eV. It is possible to see two satellite peaks in Zn 2p with binding energies of around 1026.14 and 1049.15 eV [53, 54]. In the XPS spectrum of Te 3d (Figure 5(b)), four characteristic peaks of Te $3d_{3/2}$ (583.21 eV), Te $3d_{5/2}$ (573.21 eV), and TiO_x (587.04 and 576.71 eV) eV were linked with metallic Te and silver ions Te^{4+}, respectively; this fits with the literature perfectly [55]. In the deconvolution O 1s spectra of 3Te-ZnO@40SCN NCs, there are two peaks that correspond to C-O and Zn-O, respectively (Figure 5(c)). At binding energies of 531.47 and 530.48 eV, these peaks were seen. In Figure 4(b), high-resolution N 1s spectra show three distinct peaks. $N-(C)_3$ and sp^2-hybridized nitrogen (C-N-C) are responsible for the N 1s peak in the CN network at 398.1 and 399.1 eV, respectively. N-H on the powder surface is often blamed for the peak at 400.69 eV. Two distinct peaks can be seen at 283.21 and 287.61 eV in the high-resolution C 1s spectra (see Figure S1a). The first is made up of graphitic carbon that has been adsorbed onto the surface of CN, and the second is made up of sp^2-bonded carbon (N-C-N) in the CN network. 3Te-ZnO@40SCN heterostructure S exhibits
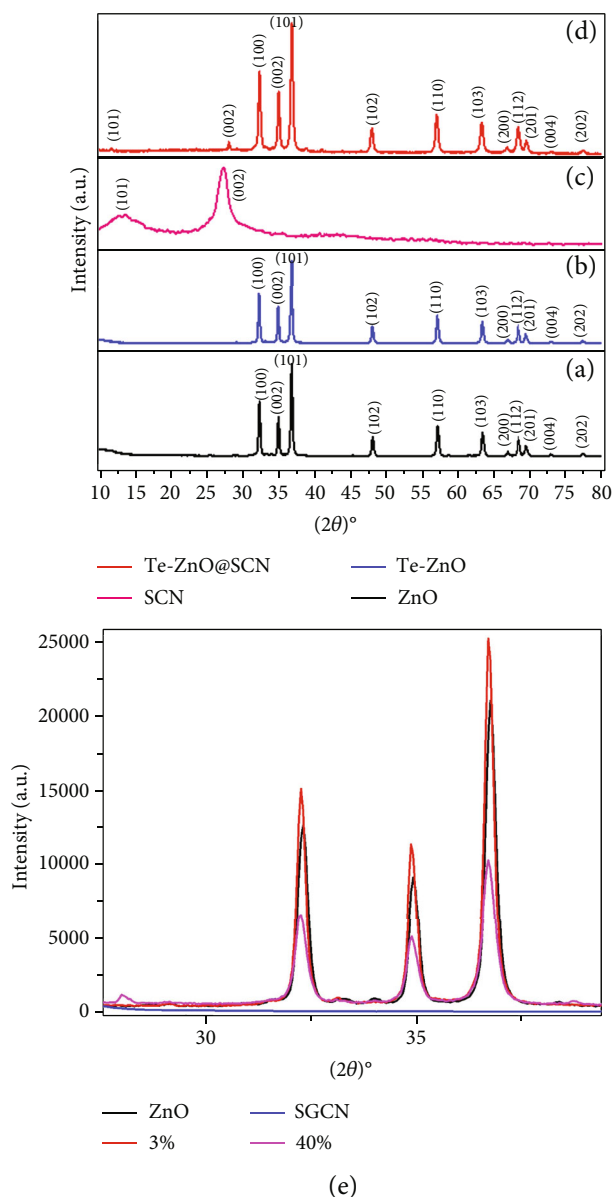
two peaks in the S 2p XPS spectra (Figure 1Sb) at 160.10 and 160.98 eV. The XPS measurements confirmed the production of the 3Te-ZnO@40SCN nanostructure and the formation of a heterointerface between Te-ZnO and SCN.

3.6. PL and BET Analyses. As shown in Figure 6(a), the photoinduced charge transfer and separation efficiency of 3Te-ZnO@40SCN NCs were investigated using PL at a 325 nm excitation wavelength. The NCs of Te-ZnO@SCN significantly lowered the surface trap-state PL of the ZnO at 565 nm (Figure 6(a)), exhibiting efficient transport and split of photogenerated e^--h^+ sets [53]. The 3Te-ZnO@40SCN NCs in this study see a decrease in electron-hole recombination, pointing to a fine heterojunction at the Te-ZnO and SCN interface. ZnO>Te-ZnO>3Te-ZnO@40SCN is the order of the studied samples' PL intensity's downward trend.
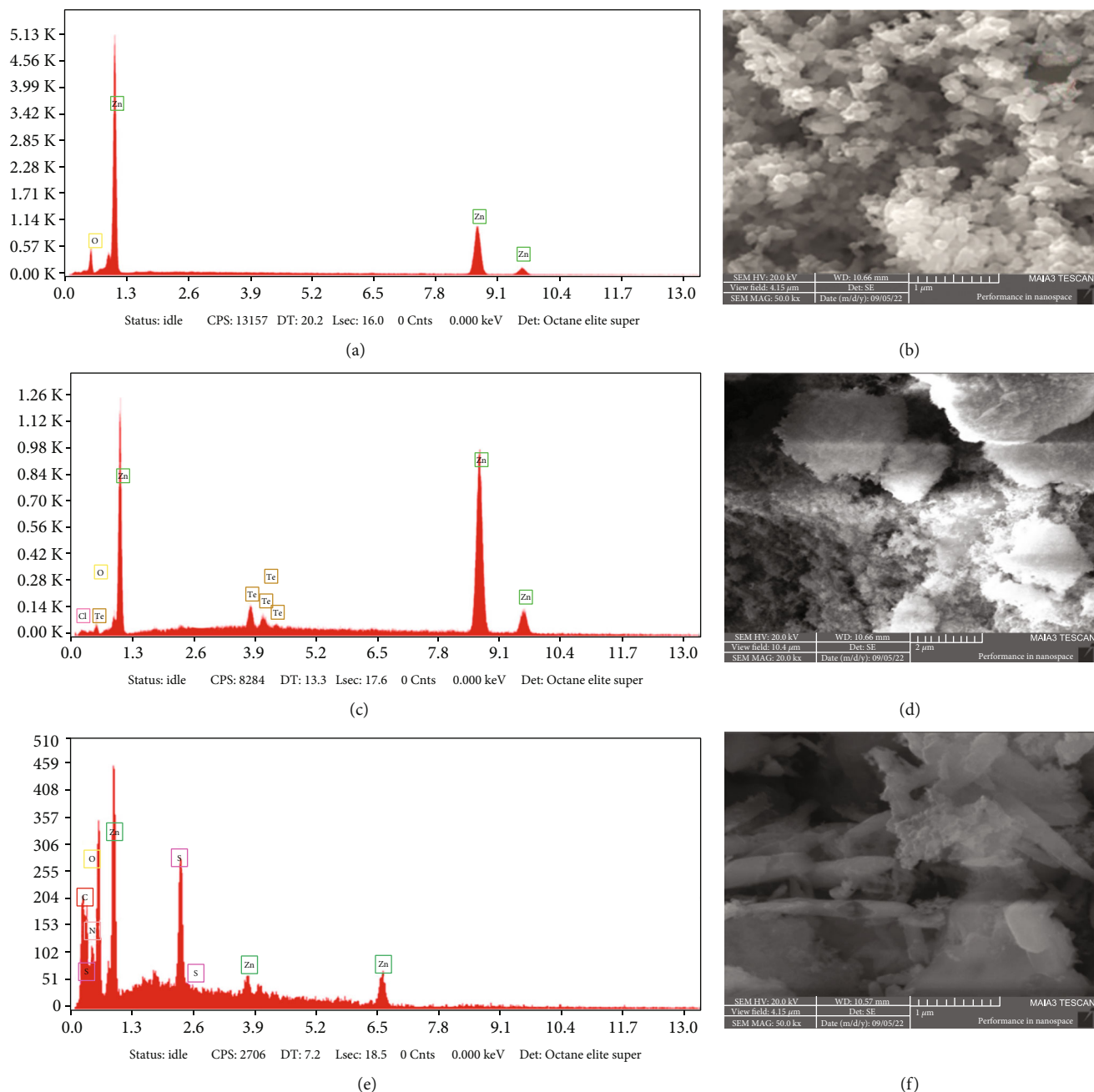
(a)

(b)

(c)

(d)

(e)

(f)

FIGURE 4: SEM-EDX analysis of (a, b) ZnO, (c, d) Te-ZnO, and (e, f) Te-ZnO@SCN.

According to the data, 3Te-ZnO@40SCN NC is enough to give increased charge carrier transport efficacy across the 3Te-ZnO@40SCN interface, leading to a very effective charge transfer technique.

For pure ZnO, Te-ZnO, and 3Te-ZnO@40SCN NCs, Figure 6(b) reveals the N_2 adsorption-desorption isotherms. It is not surprising that spherical materials like pure ZnO NPs, Te-ZnO, and 3Te-ZnO@40SCN NCs have specific surface areas of up to 5.73, 17.13, and 51.97 m^2/g, correspondingly. The surface area of 3Te-ZnO@40SCN NCs is greater than that of pure ZnO and Te-ZnO because various hybridization materials can aid in the formation of additional surface-active sites. The photocatalytic activities of 3Te-ZnO@40SCN NCs are improved by the ability of mesoporous 3Te-ZnO@40SCN NCs to effectively reduce photoinduced e^--h^+ pair recombination processes.

3.7. Photocatalytic Ability. Under the influence of sunlight, the photocatalytic ability of constructed samples was assessed. First, as shown in Figure 7(a), the photocatalytic activities of produced nanoparticles (ZnO and Te-ZnO) were investigated employing an aqueous MB solution outdoors. The deterioration contours (Figure S2) and percent degradation plots make this abundantly obvious (Figure 7(b)) that increasing the Te+4 doping up to 3 percent wt. boosted the photocatalytic activity of Te-ZnO NPs, which afterwards
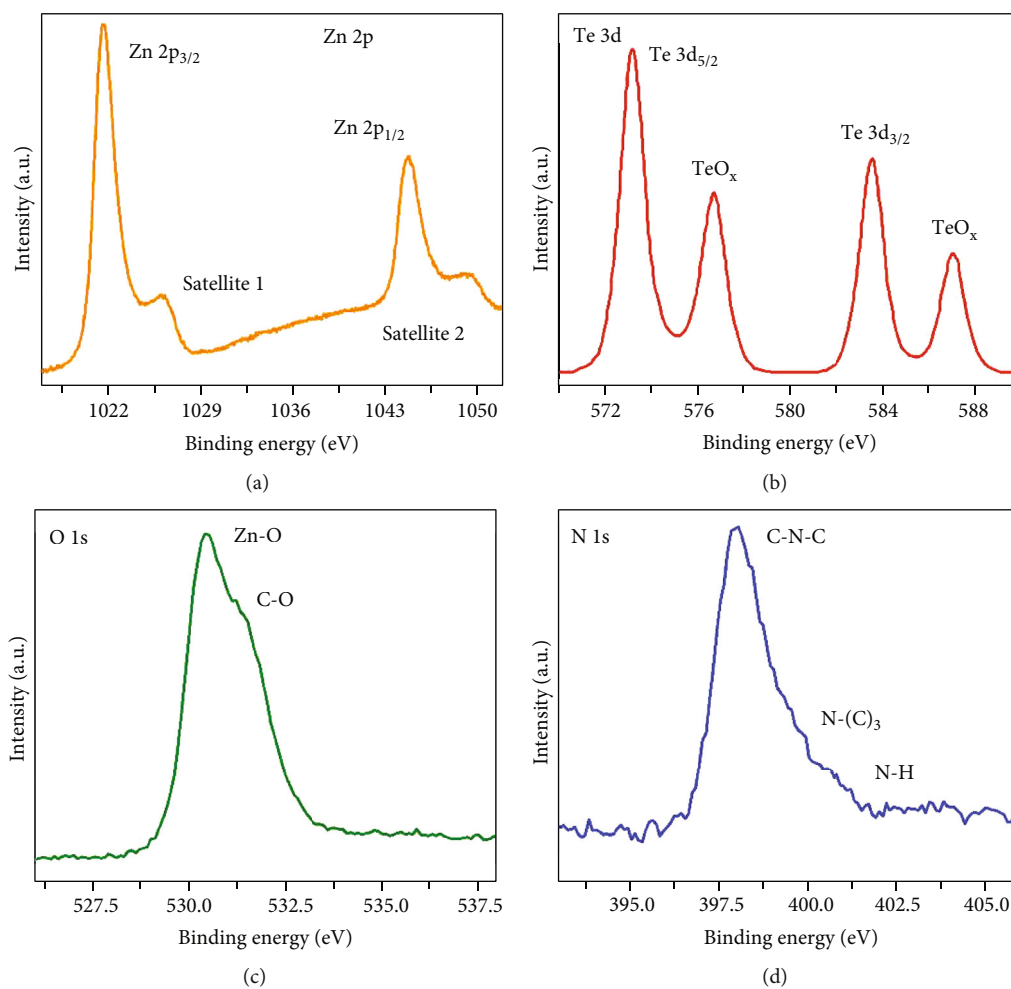
Figure 5: High-resolution XPS spectra of Te-ZnO@SCN: (a) Zn 2p, (b) Te 3d, (c) O 1s, and (d) N 1s.
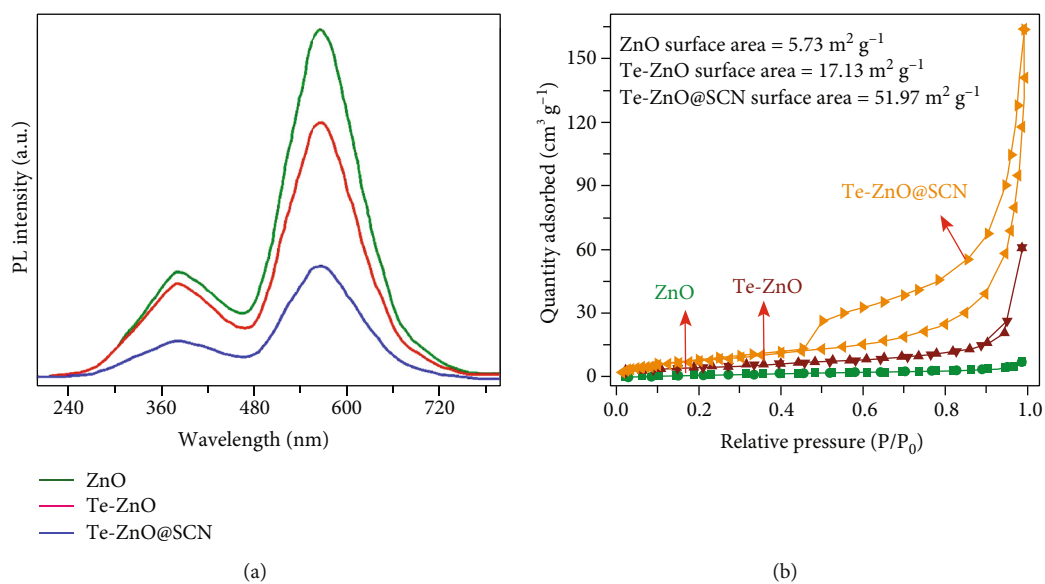

Figure 6: (a) PL spectra and (b) N_2 adsorption-desorption isotherms of Te-ZnO, ZnO, and Te-ZnO@SCN NCs.
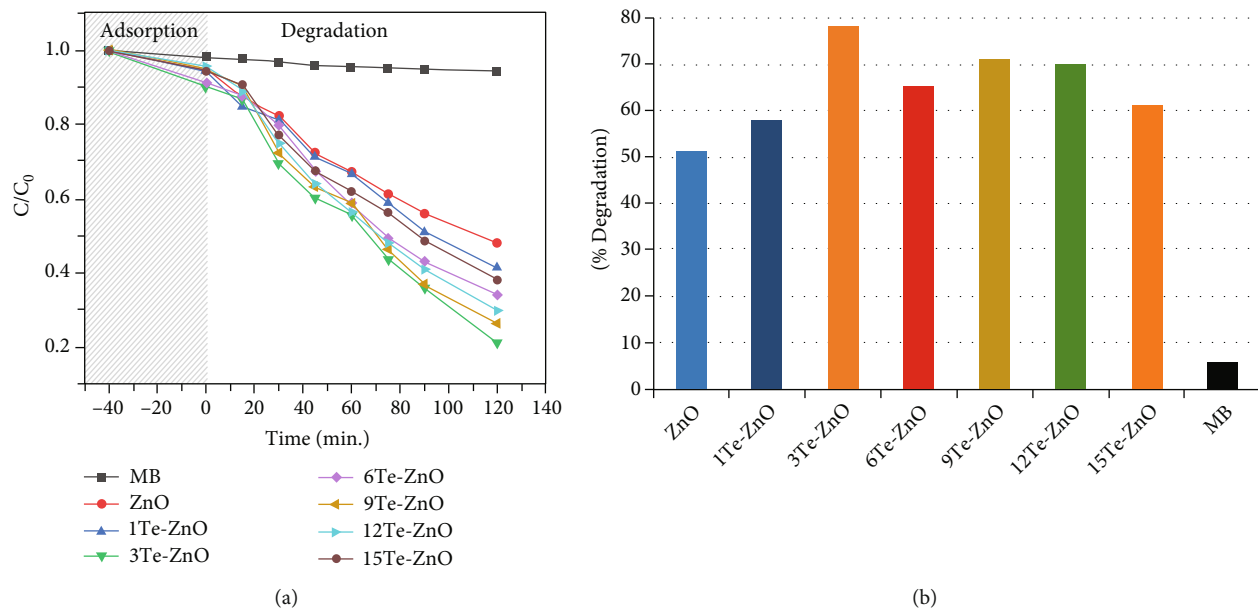
(a)

(b)

FIGURE 7: Degradation rate (a) and % degradation (b) of MB by ZnO and Te-ZnO NPs.

TABLE 1: The Te-ZnO@SCN nanocomposites' rate constant (k) values.

Sr. no.	Nanocomposites	S-g-C$_3$N$_4$ (wt%)	% degradation	k (min^{-1})
1	S-g-C$_3$N$_4$	100	51	0.0145
2	ZnO	—	54	0.0133
3	Te-ZnO@20SCN	20	65	0.0251
4	Te-ZnO@40SCN	40	89	0.0323
5	Te-ZnO@60SCN	60	100	0.0242
6	Te-ZnO@80SCN	80	85	0.0236

reduced up to 15 percent wt. Since Te^{4+} doping reduces Te-ZnO NPs' bandgap and makes the e/h$^+$ pair easier to form, Te-ZnO NPs have improved photocatalytic ability than ZnFe$_2$O$_4$. It has been shown that doping pure ZnO with different metal ions may change its optical and structural characteristics and raise the metal-doped ZnO's photocatalytic efficiency [56]. Therefore, Te (3 wt%) is the ideal doping content for Te-ZnO NPs, and while the content of doped Te^{4+} ions is raised above this level (3 wt%), Te-ZnO NPs' photocatalytic activity is reduced (Figures 7(a) and 7(b)). After 120 minutes, 3Te-ZnO NPs and ZnO NPs showed the highest (78%) and lowest (51%) photocatalytic activity, respectively. In comparison to other NPs, the 3Te-ZnO NPs had the best photocatalytic efficiency.

The 3Te-ZnO NPs were then homogenised with various concentrations of S-g-C3N4 (as listed in Table 1) to create Te-ZnO@SCN NCs, and their photocatalytic effectiveness toward MB was assessed. Before exposure to sunlight, the NCs were left in the dark to create a symmetry between dye and photocatalysts [35]. Figures 7(a) and 7(b) show that the photocatalysts only absorbed a little amount of MB. The 3Te-ZnO@40SCN NCs showed the highest dye degradation when compared to the other samples after samples were subjected to sunlight. The photocatalytic performance increased

as the SCN nanosheet loading increased from 20 to 40%, as shown by the degradation curves (Figure S3) and percentage removal plots (Figures 8(a) and 8(b)), before declining for NCs containing the SCN more than 40%. Better charge separation and more excellent visible light absorption of the Te-ZnO@SCN are primarily responsible for this enhanced degradation outcome. Thus, according to the current research, the ideal S-g-C$_3$N$_4$ concentration was found to be 40% (wt%), and Te-ZnO@SCN NC was able to degrade ≈96% MB in 90 minutes. It is most likely due to the effective junction of S-g-C$_3$N$_4$ with ZnO. However, increasing the S-g-C$_3$N$_4$ concentration beyond 40% may provide extra e-h pair recombination centers, reducing the photocatalytic efficiency. To better understand this justification, additional research is necessary [57–59]. The degradation efficiencies of the synthesized ZnO, SCN, and Te-ZnO@ (20, 40, 60, and 80 wt%) SCN NCs after 90 minutes of exposure to sunshine are 62%, 67%, 91%, 96%, 88%, and 82%, respectively. The percent photocatalytic removal of MB by comparable NCs is shown in Figure 7(b).

The kinetics of Te-ZnO/(0, 20, 40, 60, and 80 wt%) SCN NCs were realized using the Langmuir-Hinshelwood model, and the corresponding results are shown graphically in Figure S4 [38]. According to the kinetic investigation, the
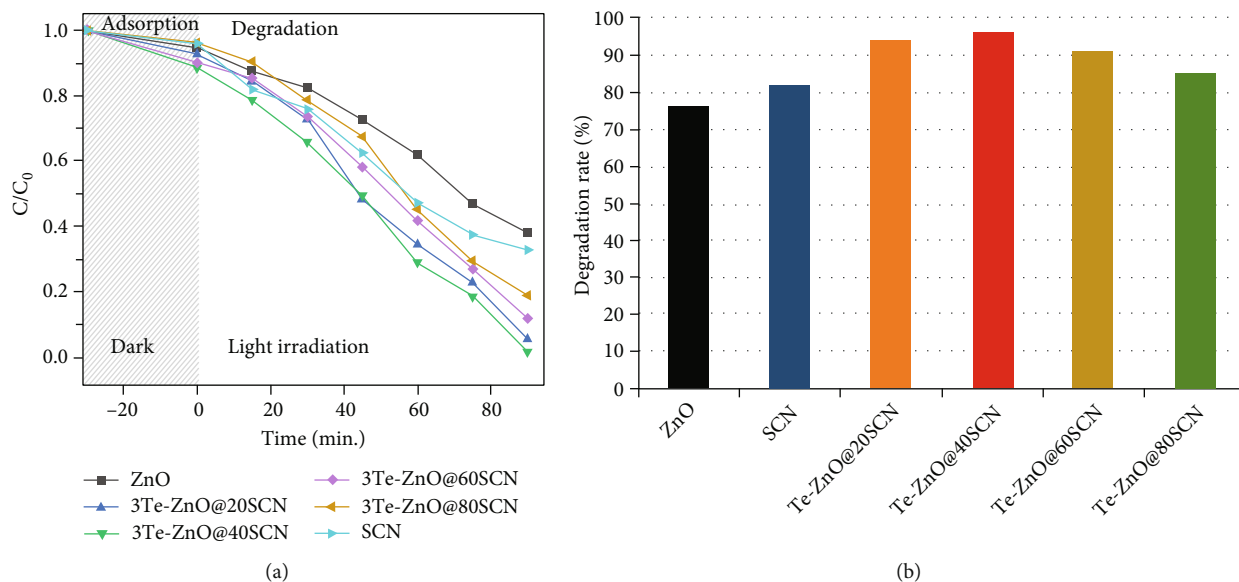
FIGURE 8: Photocatalytic removal rate (a) and % degradation (b) of MB by ZnO, SCN, and Te-ZnO@SCN NCs.

TABLE 2: Comparison of the 3Te-ZnO@40SCN NC's photocatalytic effectiveness with some earlier reports.

Sr. no.	Photocatalysts	Light sources	Contaminants	Radiation time (minutes)	Degradation percentage	Reference
1	TiO_2/GO	Solar	MB	140	97.5	[70]
2	$Bi_2WO_6/CoFe_2O_4$	Solar	Bisphenol A	120	92.0	[71]
3	$ZnNd_xFe_{2-x}O_4$	Xe lamp	Rhodamine B	180	98.0	[72]
4	$ZnFe_2O_4$	Xe lamp	Toluene	300	57.2	[73]
5	$Cu_2O/BiVO_4$	Visible	MB	180	73.0	[61]
5	$Pt-BiFeO_3$	Solar	MG	240	96.0	[62]
7	$Mn–ZnO/RGO$	Visible	RhB	140	99.0	[63]
8	$ZnFe_2O_4@ZnO$	Visible	MO	240	95.0	[64]
9	$Ag/g-C_3N_4/LaFeO_3$	Visible	MB	90	98.97	[40]
10	$3Te-ZnO@40S-g-C_3N_4$	Solar	MB	90	96.0	Present work

NCs' degradation of MB in the presence of sunlight is fit to a first-order function. Table 1 lists the rate constant (k) values of Te-ZnO@ (0, 20, 40, 60, and 80 wt%) SCN NCs.

Thus, the highest and lowest estimated "k" values were determined to be, respectively, for 3Te-ZnO@40 percent SCN NCs (0.0323 min^{-1}) and ZnO (0.0133 min^{-1}). The MB (96%) was decoloured by the 3Te-ZnO@40 percent SCN NCs in 90 minutes, and their "k" values were 2.4 and 2.3 times higher than those of ZnO and SCN correspondingly. A further increase in concentration may lead to the production of e-h pair sequence centers, which would progressively lower the photocatalytic efficacy of NCs. The observed optimal concentration of SCN for Te-ZnO/SCN NCs is 40%. Additionally, earlier investigations provide support for the current findings [35, 60]. Additional research is necessary to thoroughly investigate this justification. Comparing 3Te-ZnO@40SCN NC's photocatalytic efficiency to that of other previously reported research, there is a significant difference (Table 2) [61–68]. It is possible that the improvement in the NC's photocatalytic effectiveness over previously reported
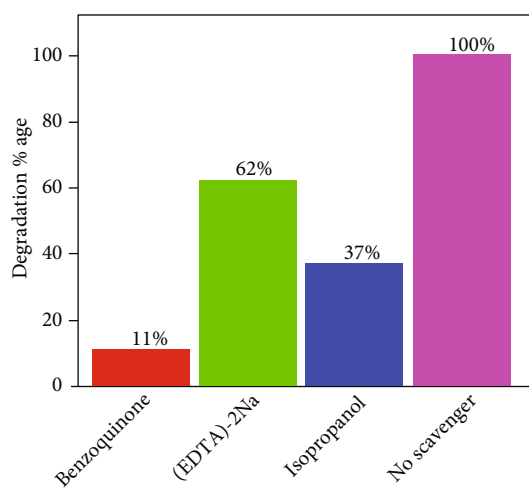

FIGURE 9: Radical scavengers' function in the photocatalytic MB degradation by 3Te-ZnO@40SCN NC.
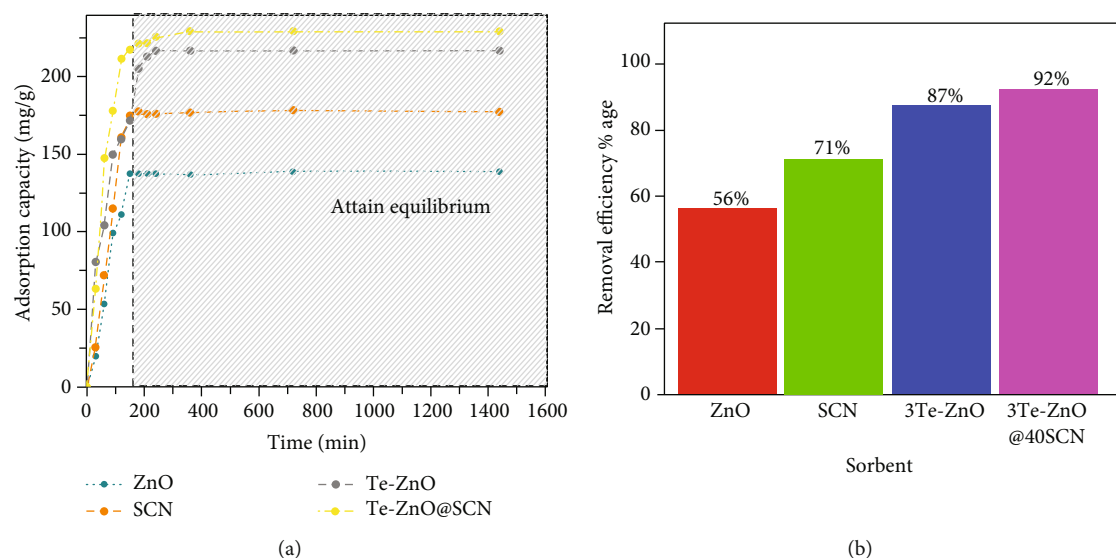
(a)

(b)

FIGURE 10: Adsorption capacity $mg\,g^{-1}$ (a) and removal efficiency % age of Cr ion (b) by using ZnO, SCN, Te-ZnO, and Te-ZnO@SCN.

TABLE 3: The adsorption of Cr(VI) ions onto artificial nanoparticles' kinetic characteristics.

Sorbents	q_e (mg g^{-1}) Experimental	Pseudo-first-order kinetics				Pseudo-second-order kinetics			
		Intercept	Slope	K_1(min^{-1})	q_e(mg g^{-1})	Intercept	Slope	K_2(min^{-1})	q_e(mg g^{-1})
ZnO	139	-0.0082	3.70904	0.005151	0.9918	0.39865	0.00636	0.000101	157
SCN	191	-0.0037	4.26447	0.005923	0.9963	0.30464	0.00495	0.000101	202
3Te-ZnO	217	-0.0031	4.68136	0.006502	0.9969	0.15382	0.00424	0.000117	235
3Te-ZnO@40SCN	229	-0.0035	4.42391	0.006144	0.9965	0.11323	0.00414	0.000151	242

composites is attributable to the formation of more excellent heterojunctions between S-g-C$_3$N$_4$ and ZnO. Additionally, the Te ions might make it easier for the NC to transfer and separate the photoinduced e/h$^+$ [25, 39, 69]. To evaluate the practicability of the 3Te-ZnO@40SCN NC, it was further employed in the recycling experiment (Figure S5).

3.8. Scavenging Activity. Organic contaminants in water are decomposed primarily by superoxide radicals ($\dot{O}_2$), hydroxyl radicals ($\dot{O}H$), and photogenerated holes (h$^+$) [65]. To test Te-ZnO@S-g-C3N4 NC's ability to produce active species, scavengers were added to dye solutions containing the photocatalyst. Benzoquinone (BQ) traps superoxide radicals ($\cdot O_2$), ethylenediaminetetraacetic acid-(EDTA-) 2Na catches hydroxyl ions (h$^+$), and isopropanol (IPA) scavenges $\dot{O}H$. The efficiency of MB breakdown was reduced by 89% with the addition of benzoquinone. Only 63% and 38%, respectively, of the breakdown rates of MB were reduced by IPA and EDTA-2Na. Figure 9 details how trapping compounds affect dye degradation reactions. Thus, in the photocatalytic dye degradation process, $\dot{O}H$ and $\dot{O}_2$ are more reactive than holes (h$^+$).

3.9. Adsorption Activity. The effect of time on chromium adsorption was assessed using various sorbents (ZnO, 3Te-ZnO, SCN, and 3Te-ZnO@40SCN). The synthesized dopant and composite significantly boosted the adsorption capacity.

The adsorption capacity showed a consistent uptrend when ZnO defects were covered by the formation of composite (3Te-ZnO@40SCN), as shown in Figure 10(a). A clear increase in the removal efficiency percentage of chromium ions was being observed by using sorbents (Figure 10(b)). The trend noted was 3Te-ZnO@40SCN>3Te-ZnO>ZnO, which was comparable to that of photocatalysts.

It is well known that too little time must pass between the sorbent and the adsorbate in order for the sorbent to reach its maximum adsorption capacity. A prolonged contact period will be ineffective. Using sorbents and a particular concentration of chromium salt solution, the adsorption time range of 30–1440 min was examined in order to calculate adsorption capacities. Cr(VI) adsorption started off moving along very quickly. Due to the surface pore channels, surface functional groups, and adequate amounts of the sorbent, numerous binding sites can be provided during the initial sorption stage, allowing heavy metal ions to connect to the material's surface with ease. However, as time goes on, these sites diminish and the electrostatic repulsion between the ions increases, making it more challenging for the adsorption reaction to reach adsorption equilibrium [66]. The synthesized sorbents attained the adsorption equilibrium within 120 to 150 minutes of adsorption (Figure 10(a)).

3.9.1. Adsorption Kinetics. Table 3 includes the experimental equilibrium adsorption capacity q_e for chromium metal ions
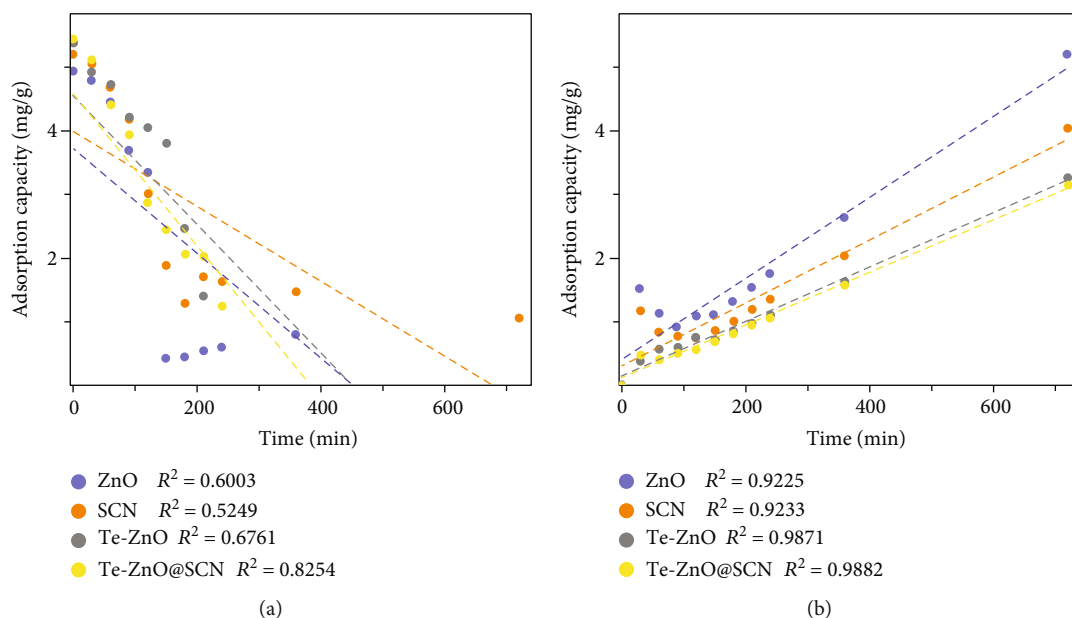
FIGURE 11: Pseudo-first-order (a) and pseudo-second-order (b) adsorption kinetic curve of chromium by using ZnO, SCN, Te-ZnO, and Te-ZnO@SCN.

at a starting concentration of $50\,mg\,L^{-1}$, the pseudo-first-order rate constants k_1 and k_2, expected equilibrium adsorption capacity q_e, and theoretical equilibrium adsorption capacity q_e. The actual values of q_e were clearly different from the theoretical values of q_e calculated from the pseudo-first-order kinetic model. The theoretical q_e values determined for the pseudo-second-order kinetic model are quite similar but not identical. Additionally, the pseudo-second-order model has a higher correlation value (R^2) than the pseudo-first-order model, suggesting that it is more widely used (Figure 11(a)). The initial chromium ion adsorption rate (h) was calculated using the pseudo-second-order rate equation, and it was found to be $2.51\,mg\,g^{-1}$ for ZnO, $6.50\,mg\,g^{-1}$ for Te-ZnO, $3.28\,mg\,g^{-1}$ for SCN, and $8.82\,mg\,g^{-1}$ for Te-ZnO@SCN. This indicates that the composite was utilized as the sorbent to produce the higher chromium adsorption rate. This revealed that the total kinetics of the chromium ion adsorption reaction is a pseudo-second-order process (Figure 11(b)), and the use of composite as a sorbent led to the highest values of the correlation coefficients (R^2), equilibrium adsorption capacity $q_{e(\text{theoretical})}$, and initial adsorption rate (h) [66, 67].

4. Mechanism for Catalytic Degradation

According to the schematic sketch, the formation of e^-/h^+ pairs in the synthesized samples is responsible for the photocatalytic destruction of MB by the manufactured NCs (Figure 12 and Figure S6). ZnO and SCN are both stimulated by sunlight when it strikes 3Te-ZnO@40SCN, and their corresponding bands (conduction bands (CB) or valence bands (VB)) form e/h$^+$ couples as a result [68]. Since the conduction band of SCN has a lower potential than the conduction band of ZnO, the photoinduced electrons can readily move from the conduction band of
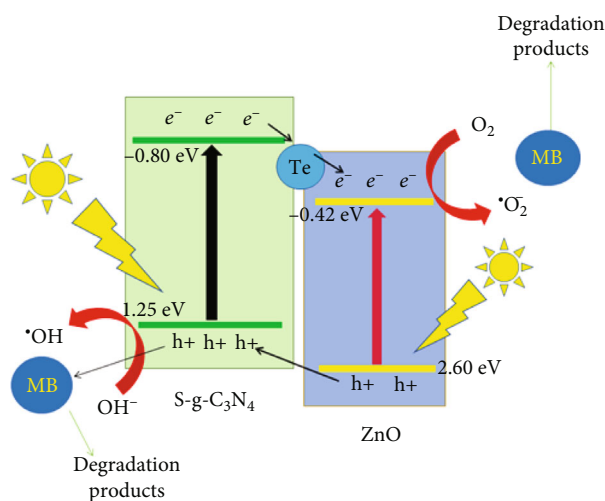

FIGURE 12: Catalytic degradation mechanism of MB by the 3Te-ZnO@40SCN NCs.

SCN to the conduction band of SCN due to the edge potentials of CB/VB. Additionally, the potential exists for the holes produced in the VB of SCN to move toward ZnO [74]. Te atoms are present in the heterostructure, which lowers the value of Eg while also facilitating the transfer of electrons from SCN to ZnO. Thus, as shown by the EIS data, Te doping has the ability to lower the charge recombination rate by increasing the spacing of photogenerated e^-/h^+ couples (Figure S7). Reactive oxygen species (O_2 and $^-$OH) are created when the e^-/h^+ pairs contact with the water molecules and oxygen on the photocatalyst surface (ROS) [75]. The MB is then degraded by an oxidative process, using up the produced radicals.

TABLE 4: When utilized in the agar well diffusion technique, ZnO, Te-ZnO NPs, SCN, and 3Te-ZnO@40SCN NCs show zones of inhibition for their antifungal activity.

Bacterial strains	Antifungal performance		
	Samples	Blank	Zone of inhibition (mm)
Alternata sp.	ZnO	0	21.6
	Te-ZnO	0	30.7
	SCN	0	24.8
	Te-ZnO@SCN	0	47.4
Bacillus sp.	ZnO	0	18.3
	Te-ZnO	0	28.4
	SCN	0	21.4
	Te-ZnO@SCN	0	41.5

5. Antifungal Activity

Further testing was done on the antifungal effectiveness of ZnO, Te-ZnO NPs, SCN, and 3Te-ZnO@40SCN NCs using the agar well diffusion technique and amphotericin B as a reference. The results are presented in broad strokes in Table 4. The highest zone inhibition values of 3Te-ZnO@40SCN for *Alternata* sp. and *Bacillus* sp. are 47.4 mm and 41.5 mm, correspondingly, based on the antifungal activity data (Table 4). They quickly penetrate the fungal cell membrane, bind to functional protein groups and phosphorus- and sulfur-containing materials, such as DNA, and ultimately cause fungal cell death owing to the 3Te-ZnO@40SCN NCs with well-defined heterojunction. 3Te-ZnO@40SCN NCs and a clearly defined heterojunction worked together synergistically to boost the antifungal effect on *Alternata* sp. and *Bacillus* sp.

6. Conclusion

Conclusively, the purpose of the current work was to synthesize ZnO NPs, Te-ZnO NPs, and Te-ZnO@SGCN NCs using a simple coprecipitation method. FTIR, SEM, EDX, and XRD patterns confirm the chemical purity and elemental compositions of synthesized samples. The photocatalytic performance of the produced samples was evaluated against MB (aqueous solution), and it was discovered that 3Te-ZnO NPs and 3Te-ZnO@40SCN NCs had extraordinarily high catalytic efficiencies. The 3Te-ZnO@40SCN was shown to degrade MB using holes, electrons, and ROS in the radical scavenging experiment. The nanocomposites demonstrated exceptional stability with a steady high degree of MB degradation for 6 consecutive catalytic cycles. Based on EIS measurements, it is possible that the creation of the synergistic interaction and fine interfaces between the Te and ZnO will considerably increase the movement and transportation of photoinduced e^-/h^+ pairs in 3Te-ZnO@40SCN. The adsorption capacity of the synthesized samples was examined via Cr ion adsorption experiments. The results and kinetic models indicate that the adsorption of chromium ions was increased by Te doping into ZnO and composite formation (Te-ZnO@40SCN). As a result, the 3Te-ZnO@40SCN

heterojunction is a suitable candidate and may be used in the photocatalytic elimination of heavy metal (Cr) and mineralization of organic contaminants (MB) to purify water.

Data Availability

On reasonable request, the corresponding author will provide the datasets collected and/or evaluated during the present study.

Conflicts of Interest

No conflict of interest is disclosed by the authors.

Acknowledgments

Supplementary Materials

In the supplementary, we described (i) material characterizations; (ii) photocatalytic degradation of MB experiments; (iii) adsorption study of heavy metal ions; (iv) the MB degradation contour of ZnO and Te-ZnO NPs; (v) photodegradation of MB by ZnO, SCN, and Te-ZnO@SCN NCs under sunlight irradiation for 90 minutes (degradation contours); (vi) kinetic characteristics of ZnO, SCN, and Te-ZnO@SCN NCs against MB; (vii) 7 consecutive MB photodegradation experiments and the cyclic stability of 3Te-ZnO@40S-g-C_3N_4 NCs; (viii) valence-band XPS spectra; and (ix) EIS Nyquist plots. (*Supplementary Materials*)

References

[1] P. Kalisamy, M. Lallimathi, M. Suryamathi, B. Palanivel, and M. Venkatachalam, "ZnO-embedded S-doped g-C3N4heterojunction: mediator-free Z-scheme mechanism for enhanced charge separation and photocatalytic degradation," *RSC Advances*, vol. 10, no. 47, pp. 28365–28375, 2020.

[2] B. Palanivel, M. Shkir, T. Alshahrani, and A. J. D. Mani, "Novel NiFe$_2$O$_4$ deposited S-doped g-C$_3$N$_4$ nanorod: Visible-light-driven heterojunction for photo-Fenton like tetracycline degradation," *Diamond and Related Materials*, vol. 112, article 108148, 2021.

[3] H. Anwer, A. Mahmood, J. Lee, K.-H. Kim, J.-W. Park, and A. C. J. N. R. Yip, "Photocatalysts for degradation of dyes in industrial effluents: Opportunities and challenges," *Nano Research*, vol. 12, no. 5, pp. 955–972, 2019.

[4] M. A. Chia and R. I. Musa, "Effect of indigo dye effluent on the growth, biomass production and phenotypic plasticity of Scenedesmus quadricauda (Chlorococcales)," *Anais da Academia Brasileira de Ciências*, vol. 86, no. 1, pp. 419–428, 2014.

[5] K. Rehman, T. Shahzad, A. Sahar et al., "Effect of reactive black 5 azo dye on soil processes related to C and N cycling," *PeerJ*, vol. 6, article e4802, 2018.

[6] B. Palanivel, M. S. Hossain, I. N. Reddy et al., "Chemical oxidants (H_2O_2 and persulfate) activated photo-Fenton like degradation reaction using sol-gel derived g-C_3N_4/$ZnCo_2O_4$ nanocomposite," *Diamond and Related Materials*, vol. 130, article 109413, 2022.

[7] P. Kalisamy, M. Lallimathi, M. Suryamathi, B. Palanivel, and M. Venkatachalam, "ZnO-embedded S-doped g-C_3N_4 heterojunction: mediator-free Z-scheme mechanism for enhanced charge separation and photocatalytic degradation," *RSC Advances*, vol. 10, no. 47, pp. 28365–28375, 2020.

[8] B. Lellis, C. Z. Fávaro-Polonio, J. A. Pamphile, and J. C. Polonio, "Effects of textile dyes on health and the environment and bioremediation potential of living organisms," *Biotechnology Research and Innovation*, vol. 3, no. 2, pp. 275–290, 2019.

[9] S. Giraldo, I. Robles, L. A. Godínez, N. Acelas, and E. Flórez, "Experimental and theoretical insights on methylene blue removal from wastewater using an adsorbent obtained from the residues of the orange industry," *Molecules*, vol. 26, no. 15, p. 4555, 2021.

[10] C. Santhosh, A. Malathi, E. Daneshvar, P. Kollu, and A. Bhatnagar, "Photocatalytic degradation of toxic aquatic pollutants by novel magnetic 3D-TiO_2@HPGA nanocomposite," *Scientific Reports*, vol. 8, no. 1, pp. 1–15, 2018.

[11] J. Zhang, Q. Xu, Z. Feng, M. Li, and C. Li, "Importance of the relationship between surface phases and photocatalytic activity of TiO_2," *Angewandte Chemie*, vol. 120, no. 9, pp. 1790–1793, 2008.

[12] J. Yu, X. Zhao, and Q. Zhao, "Effect of surface structure on photocatalytic activity of TiO_2 thin films prepared by sol-gel method," *Thin Solid Films*, vol. 379, no. 1-2, pp. 7–14, 2000.

[13] M. Bellardita, M. Addamo, A. Di Paola et al., "Photocatalytic activity of TiO_2/SiO_2 systems," *Journal of Hazardous Materials*, vol. 174, no. 1-3, pp. 707–713, 2010.

[14] J. P. Jeon, D. H. Kweon, B. J. Jang, M. J. Ju, and J. B. Baek, "Enhancing the photocatalytic activity of TiO_2 catalysts," *Advanced Sustainable Systems*, vol. 4, no. 12, article 2000197, 2020.

[15] S. Sakthivel, M. Hidalgo, D. Bahnemann, S.-U. Geissen, V. Murugesan, and A. Vogelpohl, "A fine route to tune the photocatalytic activity of TiO_2," *Applied Catalysis B: Environmental*, vol. 63, no. 1-2, pp. 31–40, 2006.

[16] V. Scuderi, G. Amiard, S. Boninelli et al., "Photocatalytic activity of CuO and Cu_2O nanowires," *Materials Science in Semiconductor Processing*, vol. 42, pp. 89–93, 2016.

[17] F. Torki and H. Faghihian, "Photocatalytic activity of NiS, NiO and coupled NiS–NiO for degradation of pharmaceutical pollutant cephalexin under visible light," *RSC Advances*, vol. 7, no. 86, pp. 54651–54661, 2017.

[18] S. P. Kim, M. Y. Choi, and H. C. Choi, "Photocatalytic activity of SnO_2 nanoparticles in methylene blue degradation," *Materials Research Bulletin*, vol. 74, pp. 85–89, 2016.

[19] A. A. Ashkarran, S. A. A. Afshar, S. M. Aghigh, and M. kavianipour, "Photocatalytic activity of ZrO_2 nanoparticles prepared by electrical arc discharge method in water," *Polyhedron*, vol. 29, no. 4, pp. 1370–1374, 2010.

[20] D. Ke, H. Liu, T. Peng, X. Liu, and K. Dai, "Preparation and photocatalytic activity of WO_3/TiO_2 nanocomposite particles," *Materials Letters*, vol. 62, no. 3, pp. 447–450, 2008.

[21] R. Lehru, J. Radhanpura, R. Kumar et al., "Studies on electrical properties of Fe doped ZnO nanostructured oxides synthesized by sol-gel method," *Solid State Communications*, vol. 336, article 114415, 2021.

[22] V. Vaiano, C. A. Jaramillo-Paez, M. Matarangolo, J. A. Navío, and M. del Carmen Hidalgo, "UV and visible-light driven photocatalytic removal of caffeine using ZnO modified with different noble metals (Pt, Ag and Au)," *Materials Research Bulletin*, vol. 112, pp. 251–260, 2019.

[23] R. Ebrahimi, K. Hossienzadeh, A. Maleki et al., "Effects of doping zinc oxide nanoparticles with transition metals (Ag, Cu, Mn) on photocatalytic degradation of direct blue 15 dye under UV and visible light irradiation," *Journal of Environmental Health Science and Engineering*, vol. 17, no. 1, pp. 479–492, 2019.

[24] H. Ren, P. Koshy, W.-F. Chen, S. Qi, and C. C. Sorrell, "Photocatalytic materials and technologies for air purification," *Journal of Hazardous Materials*, vol. 325, pp. 340–366, 2017.

[25] M. A. Qamar, S. Shahid, M. Javed et al., "Fabricated novel g-C_3N_4/Mn doped ZnO nanocomposite as highly active photocatalyst for the disinfection of pathogens and degradation of the organic pollutants from wastewater under sunlight radiations," *Colloids and Surfaces A: Physicochemical and Engineering Aspects*, vol. 611, article 125863, 2021.

[26] A. Iribarren, P. Fernández, and J. Piqueras, "Cathodoluminescence study of Te-doped ZnO microstructures grown by a vapour–solid process," *Journal of Materials Science*, vol. 43, no. 8, pp. 2844–2848, 2008.

[27] A. Iribarren, P. Fernández, and J. Piqueras, "Recombination processes in Te-doped ZnO microstructures," *physica status solidi (b)*, vol. 251, no. 3, pp. 683–688, 2014.

[28] S. Sönmezoğlu and E. Akman, "Improvement of physical properties of ZnO thin films by tellurium doping," *Applied Surface Science*, vol. 318, pp. 319–323, 2014.

[29] N. Shanmugam, S. Suthakaran, N. Kannadasan, and K. Sathishkumar, "Synthesis and characterization of Te doped ZnO nanosheets for photocatalytic application," *Journal of Heterocyclics*, vol. 105, pp. 15–20, 2015.

[30] S. Zhang, C. Su, H. Ren et al., "In-situ fabrication of g-C_3N_4/ ZnO nanocomposites for photocatalytic degradation of methylene blue: synthesis procedure does matter," *Nanomaterials*, vol. 9, no. 2, p. 215, 2019.

[31] M. Javed, M. A. Qamar, S. Shahid, H. O. Alsaab, and S. Asif, "Highly efficient visible light active Cu–ZnO/SgC 3 N 4 nanocomposites for efficient photocatalytic degradation of organic pollutants," *RSC Advances*, vol. 11, no. 59, pp. 37254–37267, 2021.

[32] A. Bahadur, S. Iqbal, M. Shoaib, and A. J. D. T. Saeed, "Electrochemical study of specially designed graphene-Fe3O4-polyaniline nanocomposite as a high-performance anode for lithium-ion battery," *Dalton Transactions*, vol. 47, no. 42, pp. 15031–15037, 2018.

[33] A. Bahadur, M. Shoaib, S. Iqbal, A. Saeed, M. S . Rahman, and P. A. Channar, "Regulating the anticancer drug release rate by controlling the composition of waterborne polyurethane," *Reactive and Functional Polymers*, vol. 131, pp. 134–141, 2018.

[34] S. Iqbal, M. Javed, M. A. Qamar et al., "Synthesis of Cu-ZnO/ polyacrylic acid hydrogel as visible-light-driven photocatalyst for organic pollutant degradation," *ChemistrySelect*, vol. 7, no. 1, 2022.

[35] M. Sher, S. Shahid, and M. Javed, "Synthesis of a novel ternary (g-C_3N_4 nanosheets loaded with Mo doped

ZnOnanoparticles) nanocomposite for superior photocatalytic and antibacterial applications," *Journal of Photochemistry and Photobiology B: Biology*, vol. 219, article 112202, 2021.

[36] A. Ahmad, Y. Wei, F. Syed et al., "The effects of bacteria-nanoparticles interface on the antibacterial activity of green synthesized silver nanoparticles," *Microbial Pathogenesis*, vol. 102, pp. 133–142, 2017.

[37] M. Sher, M. Javed, S. Shahid et al., "Designing of highly active g-C_3N_4/Sn doped ZnO heterostructure as a photocatalyst for the disinfection and degradation of the organic pollutants under visible light irradiation," *Journal of Photochemistry and Photobiology A: Chemistry*, vol. 418, article 113393, 2021.

[38] C. Kuang, P. Tan, A. Bahadur et al., "Dye degradation study by incorporating Cu-doped ZnO photocatalyst into polyacryl-amide microgel," *Journal of Materials Science: Materials in Electronics*, vol. 33, no. 13, pp. 9930–9940, 2022.

[39] M. A. Qamar, M. Javed, S. Shahid, and M. Sher, "Fabrication of g-C_3N_4/transition metal (Fe, Co, Ni, Mn and Cr)-doped ZnO ternary composites: excellent visible light active photocatalysts for the degradation of organic pollutants from wastewater," *Materials Research Bulletin*, vol. 147, article 111630, 2022.

[40] W. Zhang, Y. Ma, X. Zhu et al., "Fabrication of Ag decorated g-C_3N_4/LaFeO$_3$ Z-scheme heterojunction as highly efficient visible-light photocatalyst for degradation of methylene blue and tetracycline hydrochloride," *Journal of Alloys and Compounds*, vol. 864, article 158914, 2021.

[41] H. Tian, M. Liu, and W. J. A. C. B. E. Zheng, "Constructing 2D graphitic carbon nitride nanosheets/layered MoS$_2$/graphene ternary nanojunction with enhanced photocatalytic activity," *Applied Catalysis B: Environmental*, vol. 225, pp. 468–476, 2018.

[42] B. Suganya, S. Maruthamuthu, J. Chandrasekaran et al., "Design of zinc vanadate (Zn$_3$V$_2$O$_8$)/nitrogen doped multiwall carbon nanotubes (N-MWCNT) towards supercapacitor electrode applications," *Journal of Electroanalytical Chemistry*, vol. 881, article 114936, 2021.

[43] S. Vinoth, P. M. Rajaitha, A. Venkadesh, K. S. Shalini Devi, S. Radhakrishnan, and A. Pandikumar, "Nickel sulfide-incorporated sulfur-doped graphitic carbon nitride nanohybrid interface for non-enzymatic electrochemical sensing of glucose," *Nanoscale Advances*, vol. 2, no. 9, pp. 4242–4250, 2020.

[44] V. Srikant and D. R. Clarke, "On the optical band gap of zinc oxide," *Journal of Applied Physics*, vol. 83, no. 10, pp. 5447–5451, 1998.

[45] H. Lv, Y. Huang, R. T. Koodali et al., "Synthesis of sulfur-doped 2D graphitic carbon nitride nanosheets for efficient photocatalytic degradation of phenol and hydrogen evolution," *ACS Applied Materials & Interfaces*, vol. 12, no. 11, pp. 12656–12667, 2020.

[46] K. Guan, J. Li, W. Lei et al., "Synthesis of sulfur doped g-C_3N_4 with enhanced photocatalytic activity in molten salt," *Journal of Materiomics*, vol. 7, no. 5, pp. 1131–1142, 2021.

[47] F. Jamali-Sheini, R. Yousefi, M. Mahmoudian, N. A. Bakr, A. Sa, and N. M. Huang, "Facile synthesis of different morphologies of Te-doped ZnO nanostructures," *Ceramics International*, vol. 40, no. 6, pp. 7737–7743, 2014.

[48] M. M. Ba-Abbad, A. A. H. Kadhum, A. B. Mohamad, M. S. Takriff, and K. Sopian, "Visible light photocatalytic activity of Fe^{3+}-doped ZnO nanoparticle prepared via sol-gel technique," *Chemosphere*, vol. 91, no. 11, pp. 1604–1611, 2013.

[49] S. Iqbal, S. Nadeem, A. Bahadur et al., "The effect of Ni-doped ZnO NPs on the antibacterial activity and degradation rate of polyacrylic acid-modified starch nanocomposite," *JOM*, vol. 73, no. 1, pp. 380–386, 2021.

[50] M. Kotresh, M. Patil, and S. Inamdar, "Reaction temperature based synthesis of ZnO nanoparticles using co- precipitation method: detailed structural and optical characterization," *Optik*, vol. 243, article 167506, 2021.

[51] M. Sher, S. A. Khan, S. Shahid et al., "Synthesis of novel ternary hybrid g-C_3N_4@Ag-ZnO nanocomposite with Z-scheme enhanced solar light-driven methylene blue degradation and antibacterial activities," *Journal of Environmental Chemical Engineering*, vol. 9, no. 4, article 105366, 2021.

[52] A. Singh, B. P. Nenavathu, and M. Mohsin, "Facile synthesis of Te-doped ZnO nanoparticles and their morphology-dependent antibacterial studies," *Chemical Papers*, vol. 75, no. 8, pp. 4317–4326, 2021.

[53] W. Li, G. Wang, C. Chen, J. Liao, and Z. Li, "Enhanced visible light photocatalytic activity of ZnO nanowires doped with Mn^{2+} and Co^{2+} ions," *Nanomaterials*, vol. 7, no. 1, p. 20, 2017.

[54] M. A. Qamar, M. Javed, S. Shahid et al., "Designing of highly active g-C3N4/Co@ZnO ternary nanocomposites for the disinfection of pathogens and degradation of the organic pollutants from wastewater under visible light," *Journal of Environmental Chemical Engineering*, vol. 9, no. 4, article 105534, 2021.

[55] M. O. Reese, C. Perkins, J. M. Burst et al., "Intrinsic surface passivation of CdTe," *Journal of Applied Physics*, vol. 118, no. 15, article 155305, 2015.

[56] L. Peng, L. Fang, X. Yang et al., "Effect of annealing temperature on the structure and optical properties of in- doped ZnO thin films," *Journal of Alloys and Compounds*, vol. 484, no. 1-2, pp. 575–579, 2009.

[57] Z. Dai, Y. Zhen, Y. Sun, L. Li, and D. Ding, "ZnFe$_2$O$_4$/g-C_3N_4 S-scheme photocatalyst with enhanced adsorption and photocatalytic activity for uranium(VI) removal," *Chemical Engineering Journal*, vol. 415, article 129002, 2021.

[58] S. Kuai, Z. Zhang, and Z. Nan, "Synthesis of Ce^{3+} doped ZnFe$_2$O$_4$ self- assembled clusters and adsorption of chromium(VI)," *Journal of Hazardous Materials*, vol. 250-251, pp. 229–237, 2013.

[59] S. Vinoth, K. Subramani, W.-J. Ong, M. Sathish, and A. Pandikumar, "CoS$_2$ engulfed ultra-thin S-doped g-C_3N_4 and its enhanced electrochemical performance in hybrid asymmetric supercapacitor," *Journal of Colloid and Interface Science*, vol. 584, pp. 204–215, 2021.

[60] M. A. Qamar, S. Shahid, and M. Javed, "Synthesis of dynamic g-C3N4/Fe@ZnO nanocomposites for environmental remediation applications," *Ceramics International*, vol. 46, no. 14, pp. 22171–22180, 2020.

[61] S. Min, F. Wang, Z. Jin, and J. Xu, "Cu$_2$O nanoparticles decorated BiVO$_4$ as an effective visible-light-driven p-n heterojunction photocatalyst for methylene blue degradation," *Superlattices and Microstructures*, vol. 74, pp. 294–307, 2014.

[62] Z. H. Jaffari, S.-M. Lam, J.-C. Sin, H. Zeng, and A. R. Mohamed, "Magnetically recoverable Pd-loaded BiFeO$_3$ microcomposite with enhanced visible light photocatalytic performance for pollutant, bacterial and fungal elimination," *Separation and Purification Technology*, vol. 236, article 116195, 2020.

[63] R. Mohamed and A. Shawky, "CNT supported Mn-doped ZnO nanoparticles: simple synthesis and improved photocatalytic activity for degradation of malachite green dye under

visible light," *Applied Nanoscience*, vol. 8, no. 5, pp. 1179–1188, 2018.

[64] S. D. Kulkarni, S. Kumbar, S. G. Menon, K. Choudhari, and C. Santhosh, "Magnetically separable core-shell $ZnFe_2O_4@ZnO$ nanoparticles for visible light photodegradation of methyl orange," *Materials Research Bulletin*, vol. 77, pp. 70–77, 2016.

[65] B. Zhang, S. Wang, C. Qiu, Y. Xu, and J. Zuo, "Engineering carbon nitride with cyanide groups for efficient photocatalytic alcohol oxidation and H_2O_2 production-utilization of photo-generated electrons and holes," *Applied Surface Science*, vol. 573, article 151506, 2022.

[66] X. Xiao, Y. Deng, J. Xue, and Y. Gao, "Adsorption of chromium by functionalized metal organic frameworks from aqueous solution," *Environmental Technology*, vol. 42, no. 12, pp. 1930–1942, 2021.

[67] T. Sheela, Y. A. Nayaka, R. Viswanatha, S. Basavanna, and T. Venkatesha, "Kinetics and thermodynamics studies on the adsorption of Zn(II), Cd(II) and Hg(II) from aqueous solution using zinc oxide nanoparticles," *Powder Technology*, vol. 217, pp. 163–170, 2012.

[68] H. Zhang, C. Zhu, G. Zhang, M. Li, Q. Tang, and J. Cao, "Palladium modified $ZnFe_2O_4/g$-C_3N_4 nanocomposite as an efficiently magnetic recycling photocatalyst," *Journal of Solid State Chemistry*, vol. 288, article 121389, 2020.

[69] M. Sher, M. Javed, S. Shahid et al., "The controlled synthesis of g-C_3N_4/Cd-doped ZnO nanocomposites as potential photocatalysts for the disinfection and degradation of organic pollutants under visible light irradiation," *RSC Advances*, vol. 11, no. 4, pp. 2025–2039, 2021.

[70] R. Wang, K. Shi, D. Huang, J. Zhang, and S. An, "Synthesis and degradation kinetics of TiO_2/GO composites with highly efficient activity for adsorption and photocatalytic degradation of MB," *Scientific Reports*, vol. 9, no. 1, pp. 1–9, 2019.

[71] C. Wang, L. Zhu, C. Chang, Y. Fu, and X. Chu, "Preparation of magnetic composite photocatalyst $Bi_2WO_6/CoFe_2O_4$ by two-step hydrothermal method and its photocatalytic degradation of bisphenol A," *Catalysis Communications*, vol. 37, pp. 92–95, 2013.

[72] L. T. Nguyen, H. T. Nguyen, T. H. Le et al., "Enhanced photocatalytic activity of spherical Nd^{3+} substituted $ZnFe_2O_4$ nanoparticles," *Materials*, vol. 14, no. 8, p. 2054, 2021.

[73] J. Li, X. Li, Z. Yin, X. Wang, H. Ma, and L. Wang, "Synergetic effect of facet junction and specific facet activation of $ZnFe_2O_4$ nanoparticles on photocatalytic activity improvement," *ACS Applied Materials & Interfaces*, vol. 11, no. 32, pp. 29004–29013, 2019.

[74] Y. Shi, L. Li, Z. Xu et al., "Engineering of 2D/3D architectures type II heterojunction with high- crystalline g-C_3N_4 nanosheets on yolk-shell $ZnFe_2O_4$ for enhanced photocatalytic tetracycline degradation," *Materials Research Bulletin*, vol. 150, article 111789, 2022.

[75] Y. Wu, Y. Wang, A. Di, X. Yang, and G. Chen, "Enhanced photocatalytic performance of hierarchical $ZnFe_2O_4/g$-C_3N_4 heterojunction composite microspheres," *Catalysis Letters*, vol. 148, no. 7, pp. 2179–2189, 2018.